ICCCM-JOURNAL OF SOCIAL SCIENCES AND HUMANITIES
2026; 5(sp): 1-14
Published online 3 25 2026 (https://icccmjssh.com/)
doi: 10.53797/icccmjssh.v5isp.1.2026
e-ISSN 2811-4469

Comparison studies of Double Layered Hydroxides modified by sodium dodecyl sulphate and Graphene Oxide composites for the treatment of Coomassie blue (G-250) in wastewater

Rashed, S. H.[1*]

[1]Department of Chemistry, Faculty of Science. Alexandria University, P.O. Box 426, Ibrahimia, Alexandria, 21321, EGYPT

*Corresponding author: Sarahhesham729@gmail.com

To Cite This Article:
Rashed, S. H. (2026). Comparison studies of Double Layered Hydroxides modified by sodium dodecyl sulphate and Graphene Oxide composites for the treatment of Coomassie blue (G-250) in wastewater. ICCCM *Journal of Social Sciences and Humanities,* 5(Special Issue), 1-14. https://doi.org/10.53797/icccmjssh.v5iSP.1.2026

Received 19 February 2026. **Revised** 25 February 2026, **Accepted** 13 March 2026, **Available online** 25 March 2026

Abstract: In this study, Sodium Dodecyl Sulphate modified double layered hydroxides (SDS-LDH) and Graphene Oxide Double Layered Hydroxides (GO-LDH) were synthesized via reconstruction and sonochemical methods, respectively. Batch experiments were performed to study the adsorption behaviour and mechanism of the synthesized adsorbents to eliminate Coomassie brilliant blue G-250 dye (CBB) from an aqueous solution. GO-LDH was more efficient in CBB adsorption through ion exchange, resulting in q_e= 1430 mg/g using 5 mg of GO-LDH at 5 min owing to its high specific average surface area and inter-lamellar distance. However, SDS-LDH depended on the hydrophobic interaction with CBB leading to q_e= 62 mg/g using 85 mg of SDS-LDH at 60 min. SDS-LDH and GO-LDH obeyed the PSO model with a GO-LDH adsorption initial rate 7 times higher than that of SDS-LDH as discussed by the intra-particle diffusion model via three steps.

Keywords: SDS-LDH; GO-LDH; CBB (G-50); Harkins-Jura; Langmuir

1. Introduction

The world has recently been afflicted by serious water pollution. Textile, printing, and painting industries resulted in dye pollution (Abbas et al., 2016). Dyes are not only harmful to living things because of their intense colors, toxicity, mutagenicity, and carcinogenicity but also difficult to remove due to their complicated aromatic structures; water-solubility, anti-oxidative properties; and low degradability (Tang et al., 2023), (Sun et al., 2020). The evaporated chemicals caused by dyes in wastewater might affect climate change, resulting in respiratory infections, human organs damage, killing the aquatic life, increasing drought in some areas, and decreasing rain fall in other areas (Jawad et al., 2021). Various techniques were introduced for the wastewater treatment, such as: catalytic degradation (Tabana et al., 2023), advanced oxidation (Gupta et al., 2023), photocatalysis (Gohr et al., 2019), electrocatalysis (Liu et al., 2015), membrane separation (Zhao et al., 2023), and adsorption (Gohr et al., 2022). The adsorption process was the most successful method due to its simplicity, lack of environmental pollution, and low cost (Yilmaz, 2022). The anionic organic dye Coomassie brilliant blue G-250 (CBB) (triphenylmethane) is well-known for its role in protein determination and the wool industry (Lü et al., 2007), (Rayaroth et al., 2015), however it is harmful to humans, causing mucus membrane irritation, respiratory tract toxicity (Tian et al., 2023), and eye problems (Sujitha & Ravindhranath, 2016).

CBB could be removed by the adsorption process utilizing numerous adsorbents, including active carbon derived from barks of Ficus racemosa plant (Sujitha & Ravindhranath, 2016), amino-functionalized silica smart nano particles (Sabeela et al., 2019), starch/poly (alginic acid-cl-acrylamide) nanohydrogel (Sharma et al., 2017), activated carbon prepared from Nigella sativa L. waste (Abdel-Ghani et al., 2017) , snail shell powder (Ibrahim et al., 2019), wheat bran (Ata et al., 2012), apricot stone activated carbon (Abbas et al., 2016), α-chitin nanoparticles (Dhananasekaran et al., 2016), sand (Rauf et al., 2008), Fe-Pillared bentonite (PILC-Fe), Benta-Na (Kadeche et al., 2020), and CuO/C nanocomposites (Bhavyasree & Xavier, 2021). Double Layered Hydroxides (LDH-s) are considered as anionic clays (2d-materials), $[M_{1-x}^{2+}M_x^{3+}(OH_2)]^{x+}(A^{n-})_{x/n}.H_2O]$, that made up of positive cation layers ($M_{1-x}^{2+}M_x^{3+}$) bonded to hydroxyl

*Corresponding author: sarahhesham729@gmail.com

groups, intercalated with negatively charged inorganic anions $(A^{n-})_{x/n}$ and water molecules (H_2O), neutralizing its lamellae. LDH exhibited ion exchange, complexation, surface adsorption, good regeneration efficiency, high specific surface area, and no health hazard (Rashed et al., 2022), (Daud et al., 2019).

Furthermore, LDH layers could be intercalated with organic molecules rather than inorganic molecules, resulting in hydrophobic character, enhancing organic pollutant adsorption (Starukh et al., 2016). LDH-s can be synthesized using a variety of methods (Rashed et al., 2022). According to our previous work(Rashed et al., 2022), ZnAl-CO_3 LDH was used to remove Methyl Orange (MO) and CBB from an aqueous solution, but the adsorption capacity did not exceed 7.5 mg/g, which might be due to the difference in size and charge of the intercalated anion (CO_3^{2-}) corresponding to LDH interlamellar distance and that of CBB during ion exchange adsorption (Elmoubarki et al., 2021). Moreover, graphene oxide (GO) was chosen for the adsorption process due to its highly concentrated active sites (C-OH, C=O, COOH, C-O-C) forming hydrogen bonds from the inner outer layers and high specific area that led to adsorbing pollutants as heavy metals, pesticides, endocrine disrupting compounds, phenols, chlorophenols, and dyestuff from wastewater (Abu-Nada et al., 2021). It was reported that GO led to increasing the adsorption capacity due to the wide specific area of hydrogen bond interactions between GO and CBB, but only 14.5 mg/g was achieved due to the repulsion between the negative functional groups of oxygen of the GO surface and the CBB anions (Abu-Nada et al., 2021).

Herein, the LDH was synthesized using a modified reconstruction method by incorporating the organic surfactant sodium dodecyl sulphate (SDS) after calcining LDH at 500°C, yielding (SDS-LDH) of hydrophobic nature (Starukh et al., 2016). Additionally, the LDH lamellae was sonochemically grown into GO layers forming (GO-LDH). The two modified synthesized adsorbents were expected to enhance the CBB dye removal. The synthesized adsorbents were characterized and their adsorption parameters, kinetic models, isotherms, thermodynamics were assessed. Besides, recycling using the memory effect process to study the mechanism of both adsorbents towards CBB adsorption for eventual use was performed (Starukh & Levytska, 2019),(Mishra, et al.2018).

2. Methodological Framework

The used resources, preparation of the adsorbents, and characterization techniques are described in detail in the supplementary data. This supplementary information provides comprehensive methodological explanations to ensure the reproducibility of the study (Stodden et al., 2016). It also includes additional experimental conditions, materials specifications, and procedural steps that support the main findings. Furthermore, detailed characterization results are presented to give deeper insight into the properties and performance of the adsorbents. In addition, the supplementary data contain extended datasets and supporting analyses that were not included in the main text due to space limitations. These additional details help to strengthen the reliability and transparency of the research. The documentation also outlines calibration methods and quality control measures applied throughout the experiments (Abzalov, 2008). Moreover, any assumptions, limitations, and potential sources of error are clearly addressed to provide a balanced interpretation of the results. Additional Fig.s and tables are provided to visually support the data and highlight key trends observed during the study. References to standard methods and previously published protocols are also included to validate the approaches used. Detailed descriptions of instrumentation settings and analytical parameters are also presented to ensure clarity and consistency in the experimental procedures. Where applicable, comparisons with related studies are included to contextualize the findings within the broader scientific literature. Overall, the supplementary materials serve as an essential reference for readers who seek a more in-depth understanding of the experimental design and outcomes.

3. Results and Discussion

3.1. Physicochemical characterization of SDS-LDH and GO-LDH composites

Fig. 1 displayed the XRD patterns of LDH, SDS-LDH, GO and GO-LDH. The XRD pattern of LDH exhibited the basal peaks (003) and (006) at 2θ of 9.9455° and 19.936° and the non-basal peaks (012) and (110) at 2θ of 34.15° and 60.61°, respectively, referring to the good crystallinity of LDH layers. It was found that after the formation of SDS-LDH composite (003) and (006) basal peaks were shifted to higher (2θ) of 10.04° and 20.4° and their peaks intensities were significantly decreased due to the absence of CO_3^{2-} interlayered anion (Abd-Elhamid et al., 2019), (Mahjoubi, et al. 2019).

Additionally, the intensity of (012) and (110) non-basal peaks increased, indicating the enhanced crystallinity of LDH by the organic anion SDS (Ramimoghadam, et al., 2012). Besides, (100), (101), (102), (103), (200), (112), and (201) peaks appeared at (2θ) of 31.5°, 36.22°, 47.78°, 60.1°, 62.71°, 67.97°, and 70.11°, respectively owing to the perfect orientation of SDS with ZnO (Mahjoubi, et al, 2019). Therefore, SDS-LDH adsorbed CBB dye via hydrophobic interactions with SDS (Mahjoubi, et al, 2019). Moreover, in the XRD pattern of GO-LDH, the GO characteristic peak at 2θ of 10.0115º disappeared due to GO sheets dispersion between LDH layers as a result of the electrostatic attraction between the LDH metals and the oxygen functional groups of GO sheets (Rashed et al., 2022). The basal peaks (003) and (006) were also shifted to 2θ of 8.0061° and 16.094°, respectively, along with strengthening and sharpening their intensities, revealing CBB adsorption easily via anion-exchange due to high interlayered distance. In addition, new non-basal peaks (009), (015), and (113) were observed at 2θ of 25.44°, 35.54°, and 61.72°, respectively, referring to the excellent crystallinity due to the well-grown ZnO on GO sheets (Rashed et al., 2022).

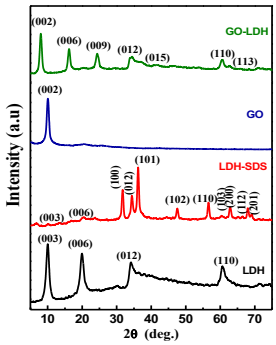

Fig. 1 - XRD patterns of LDH, SDS-LDH, GO and GO-LDH.

The morphological investigation and EDS spectra of LDH, C-LDH, SDS-LDH and GO-LDH were displayed in Fig. 2 and Fig. 3, respectively. Their corresponding specific area distribution curves were shown in Fig. S1, supplementary data. The SEM images depicted the layered arrangement of LDH with an average particle size of 2787.75 nm (Fig. 3a) and an average specific surface area of $21.2*10^6$ nm^2/g (Fig. S1a, supplementary data). After calcination, C-LDH morphology exhibited flakes with rough surface with an average particle size of 3329.867 nm (Fig. 3b) and a lower average specific surface area of $16.7*10^6$ nm^2/g (Fig. S1b) due to the removal of H_2O and CO_3^{2-} upon calcination (Starukh et al., 2016). SEM images of SDS-LDH possessed more dispersed layers of an average particle size of 2300.526 nm (Fig. 3c), due to the strong affinity of LDH to organic surfactants other than CO_3^{2-} (Kong et al., 2018). Besides, SDS increased the average specific surface area of LDH to $35.5*10^6$ nm^2/g. Whereas, incorporation of GO to LDH perfectly improved the morphological arrangement of LDH layers (Fig. 3d) owing to the well-dispersed LDH metals onto GO sheets that led to a decrease in its average particle size to 1508.667 nm a long with an increase in the average specific surface area to $47*10^6$ nm^2/g (Fig. 1Sd) (Rashed et al., 2022). The EDS results confirmed the presence of C, O, Na, Al and Zn elements in the synthesized composites, indicating the great accuracy of LDH synthesis. In case of C-LDH, both of carbon and oxygen contents decreased due to successful calcination process via CO_3^{2-} elimination (Fig. 4b). After the reconstruction of SDS-LDH, sulphur content appeared due to the sulphonyl group of SDS (Fig. 4c). Additionally, carbon content increased in SDS-LDH and GO-LDH as a result of the presence of the SDS alkyl chain and the carbon skeleton, respectively (Zhang et al., 2019).

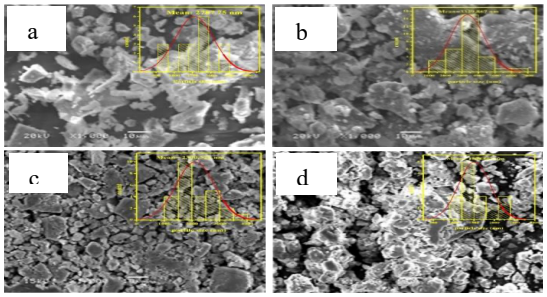

Fig. 2 - The SEM image of a) LDH, b) C-LDH, c) SDS-LDH and d) GO-LDH.

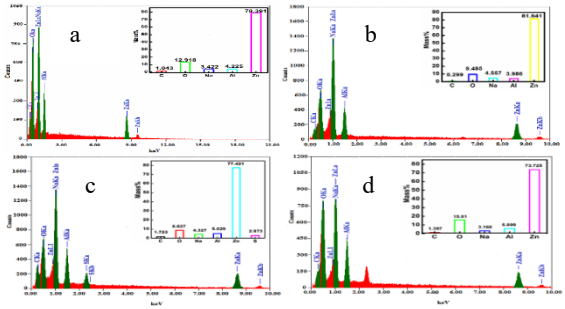

Fig. 3 - EDS spectrum of a) LDH, b) C-LDH, c) SDS-LDH and d) GO-LDH

Infrared spectra of LDH, C-LDH, SDS-LDH, GO, GO-LDH, CBB/SDS-LDH and CBB/GO-LDH were shown in Fig. 5a. The FT-IR spectrum of LDH exhibited a wide band at 3440 cm^{-1} due to the hydroxyl group vibration bond of M-O-H or H-O-H, a sharp band at 1560 cm^{-1} of water molecule bending vibration, and a band at 1385 cm^{-1} as a result of interlayered anion CO_3^{2-} stretching mode (Rashed et al., 2022). LDH calcination process led to a shifted narrow band at

3432 cm^{-1} due to the elimination of OH^- hydroxyl groups from LDH forming C-LDH. The two sharp bands at 1385 and 1560 cm^{-1} of LDH disappeared for C-LDH, proving successful calcination (Elmoubarki et al., 2021). The FT-IR spectrum of SDS-LDH exhibited sharp peaks at 2919 and 2852 cm^{-1} due to C–H (alkyl chains) stretching and bending vibrations and peaks at 1217, 1062, and 990 cm^{-1} of OSO_3^- anions stretching and bending vibrations. Besides, the peaks at 3480 and 1632 cm^{-1} of hydroxyl group stretching and water molecules bending vibrations were shifted and weakened in intensity as compared to LDH, which might be due to the decrease of the O-H bond of M-O-H or H-O-H of LDH as a result of the great affinity of LDH metals to bond with SDS anions (Starukh et al., 2016). The FT-IR spectrum of GO sheets displayed a characteristic peak at 3453 cm^{-1} of O-H vibration of OH or COOH functional groups on GO surface, a band at 1757 cm^{-1} of C-O vibration of COOH, and bands at 1633, 1410, and 1038 cm^{-1} of C-O-H, C-O-C, and C-O stretching modes of GO carbon skeleton, respectively (Rashed et al., 2022). After LDH growth on GO sheets (GO-LDH), the broad band due to the O-H vibration of hydroxyl groups and water molecules was shifted to 3495 cm^{-1} as well as the bands due to the bending interlayered water molecules and CO_3^{2-} anions were shifted to 1640 and 1385 cm^{-1}, respectively. The stretching modes of C-O-C and C-O-H were also shifted to 1430 and 1100 cm^{-1}, confirming that LDH layers were perfectly constructed on the GO sheets. The shifted bands of metal oxides also proved that the metals were well-complexed with GO oxygen functional groups (Rashed et al., 2022). Illustratively, the bands observed at 600 - 400 cm^{-1} were due to M-O-H and M-O-M vibrational modes of metal oxides of LDH, C-LDH, SDS-LDH, GO-LDH (Rashed et al., 2022), (Starukh & Levytska, 2019). After CBB adsorption by SDS-LDH, the 2 bands of the alkyl chains were shifted to 2921 and 2854 cm^{-1}, indicating hydrophobic interactions of alkyl chains with CBB (Munir et al., 2020). On the other hand, CBB adsorption by GO-LDH exhibited a significant decrease in the peak intensity of CO_3^{2-} at 1385 cm^{-1}, referring to that the interlayered space was embedded with CBB molecules. FT-IR spectra of CBB adsorption with either SDS-LDH or GO-LDH exhibited bands shift at 3511 and 3462 cm^{-1} for the hydrogen bonds and at 700–400 cm^{-1} for M-O-M and M-O-H metal oxide vibrations (Munir et al., 2020). The later shift indicated metal complexations with CBB dye for both SDS-LDH and GO-LDH (Rashed et al., 2022). The Raman spectra of the synthesized composites were displayed in Fig. 5b. For LDH, the band at 1392 cm^{-1} due to stretching mode of interlayered CO_3^{2-} as well as the two split bands at 1090 and 1060 cm^{-1} might be due to the formation of M-O symmetrical stretching bond in M-CO_3^{2-} (Rashed et al., 2022). The band at 2860 cm^{-1} was due to O-H vibration between carbonate and water molecules (Rashed et al., 2022). Raman spectrum of C-LDH revealed that the carbonate band of LDH at 1392 cm^{-1} was diminished due to the removal of CO_3^{2-}, which confirmed FTIR results. Additionally, the band at 2860 cm^{-1} of LDH completely decreased in C-LDH due to the removal of O-H bonds between CO_3^{2-} and H_2O after the calcination process (Lin et al., 2014). SDS-LDH Raman spectrum exhibited only one sharp peak at 2888 cm^{-1} due to SDS alkyl chain vibrational mode (Islam et al., 2013). The bands 800 -500 cm^{-1} were due to M-O-M and M-O-H metal oxides vibrations of C-LDH and SDS-LDH (Islam et al., 2013). Raman spectra of GO revealed 2 main bands: D-band at 1362 cm^{-1} due to disordered graphitic carbon defects and G-band at 1584 cm^{-1} due to in-plane vibration well-ordered SP^2 carbon atoms with a graphitization ratio of (I_D/I_G =1.34). Raman spectrum of GO-LDH revealed a band at 1416 cm^{-1} due to stretching mode of interlayered CO_3^{2-} and D- and G-bands were shifted to 1350 cm^{-1} and 1608 cm^{-1}, respectively, with (I_D/I_G =1.58), indicating the increase in the crystallization degree of LDH by adding GO. Whereas, the I_G was lower than that of GO due to the perfect formalization of the lamellar structure on GO surface (Rashed et al., 2022). Moreover, CBB adsorption by SDS-LDH depicted that the sharp peak of alkyl chain of SDS exhibited a Raman shift to 2992 cm^{-1} due to the hydrophobic interaction of alkyl chain of SDS with CBB. Whereas, adsorption of CBB by GO-LDH led to a Raman shift for most peaks as well as D- and G-bands were shifted to 1373 and 1587 cm^{-1}, respectively (Liang et al., 2015) , with a decreased graphitization ratio (I_D/I_G = 1.041) due to the blockage and the reduction of GO-LDH defects by CBB adsorption (Bu et al., 2021). Therefore, Raman spectra confirmed that metal oxides complexation for GO-LDH, CBB/SDS-LDH, and CBB/GO-LDH in the range of 400-1000 cm^{-1}. The CBB adsorption mechanisms concluded from FTIR and Raman spectra results were represented in the schematic diagrams Fig. S2 (supplementary data).

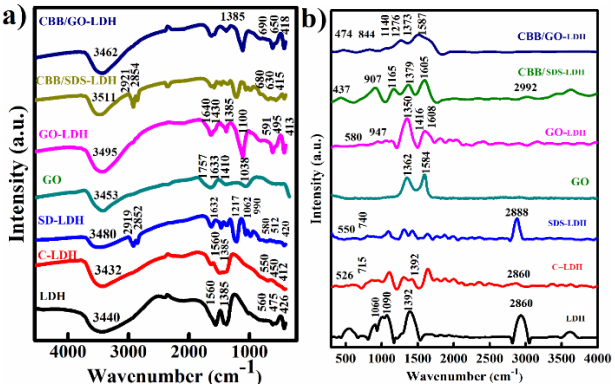

Fig. 4 - (a) FTIR Spectra and (b) Raman Spectra of LDH, C-LDH, SDS-LDH, GO, GO-LDH, CBB-SDS-LDH and CBB-GO-LDH.

The thermal stability of the synthesized composites was depicted in Fig. 6. TGA of LDH showed weight losses of 0.182 and 0.291 mg at (21.35-161.66) and (161.66-214.85) ºC, respectively, due to the removal of weakly adsorbed water and interlayered water molecules. Besides, series of processes were observed as de-hydroxylation of (M-OH) at (214.85-263.04) ºC, decarbonation at (263.04-382.53) ºC and decomposition of metal oxides (M-O-M) at (382.53-447.28) ºC. It was found that C-LDH exhibited less weight losses of 0.11 and 0.152 mg at (19.83-55.31) and (55.31-181.03) °C, respectively, of adsorbed or intercalated water as compared to LDH. Even though the de-hydroxylation, decarbonation, and decomposition of metal oxides processes were detected at (181.03-396.69) °C with weight loss of 0.071 mg. The decrease in weight loss and temperature exemplifies that LDH thermal stability decreased after calcining (Rashed et al., 2022). TGA curve of SDS-LDH displayed weight loss of 0.335 mg at (30.77-177.54) ºC attributed to the adsorbed or intercalated water molecules, followed by the decomposition of SDS species and destruction of SDS-LDH with weight loss of 1.38 mg at (177.54-619.37) °C (Rashed et al., 2022), (Danaei et al., 2018). Additionally, the de-hydroxylation and decomposition of metal oxides attributed to SO_3^{2-} exhibited weight loss of 0.052 and 0.064 mg at much higher temperatures (619.37–761.96) °C and (761.96-799.99) ºC, respectively (Sharif et al., 2020). Therefore, introducing SDS to LDH extended the temperature to higher Celsius degrees, which positively improved its thermal stability. Furthermore, TGA of GO revealed weight losses of 1.03 and 0.83 mg at (30–90) and (90-160) ºC, respectively, due to the removal of water molecules adsorbed on the external gallery of GO. The degradation processes of O-H and C-O-C functional groups led to the greatest weight loss of 1.31 mg at (160–216) °C (Rashed et al., 2022), followed by weight loss of 0.428 mg of COOH decomposition at (216–300) ºC (Rashed et al., 2022). TGA of GO-LDH had increased weight loss of 0.836 mg at (31.61–166.79) °C due to the increased external and interlayered water molecules of GO-LDH. Consequently, GO-LDH species declined at high temperatures of (166.79–341.09) ºC due to the elimination of oxygen-functional groups with weight loss of 0.601 mg. Besides, TGA of GO-LDH exhibited de-hydroxylation and decarbonation with weight losses of 0.221 and 0.227 mg at (341.09–549.19) and (549.19–745.13) ºC (Kong et al., 2018), respectively, along with decomposition of M-O-M with weight loss of 0.085 mg at (745.13–799.99) ºC, indicating the high thermal stability of GO-LDH at high temperatures.

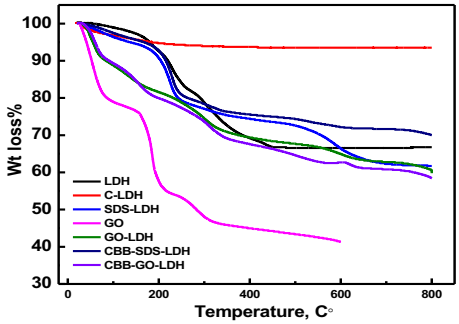

Fig. 5 - TGA curves of LDH, C-LDH, SDS-LDH, GO and GO-LDH.

According to the Zeta-sizer size distribution curves (Fig. 6a and b), the average size of SDS-LDH was 729.9 nm, which was much higher than that of GO-LDH (385.9 nm), resulting in a higher surface area of GO-LDH and thus a higher polydispersity index of GO-LDH (0.406) than that for SDS-LDH (0.34), leading to higher adsorption efficiency of GO-LDH than SDS-LDH. These results fit with the average size particle and average specific surface area calculations obtained from SEM (Danaei et al., 2018). The zeta potentials of SDS-LDH and GO-LDH were -12 and +16.8 mV, respectively, as displayed in Fig. 7c and d. According to Fig. 7e, the adsorption capacity of SDS-LDH decreased as its initial pH increased with maximum q_e of 47 mg/g (pH = 1.5 and 3) owing to the increased positive charges on the adsorbent surface that attract the negative charges of CBB dye. The decrease in the adsorption capacity of SDS-LDH above (pH = 7) was due to the increase of OH^- anions on its surface [1]. However, the maximum adsorption capacity of GO-LDH was 62 mg/g at weak acidic medium (pH = 5.5) as stated for LDH-like materials (Rashed et al., 2022), (Sharif et al., 2020). The adsorption capacity decreased below and above (pH = 5.5) as a result of GO-LDH metal dissolution in acidic and basic media (Rashed et al., 2022), (Zaghouane-Boudiaf et al., 2012). From Fig. 7f, the point of zero charge (PZC) of SDS-LDH was 7.6, which was less than that of GO-LDH (7.9) due to the higher negativity of SDS-LDH than GO-LDH. According to the relationship between initial pH (pHi) and final pH (pH_F), Fig. 7g, it was found that below (pHi =7), $pH_F > PH_i$ due to the partial protonation of LDH, whereas above ($pH_i = 7$), pH_F was in the range of (7.7 to 8.2) and (7.5 to 8.5) for SDS-LDH and GO-LDH, respectively, due to the buffering adsorption capacity on the adsorbent (Ai., et al (2011).

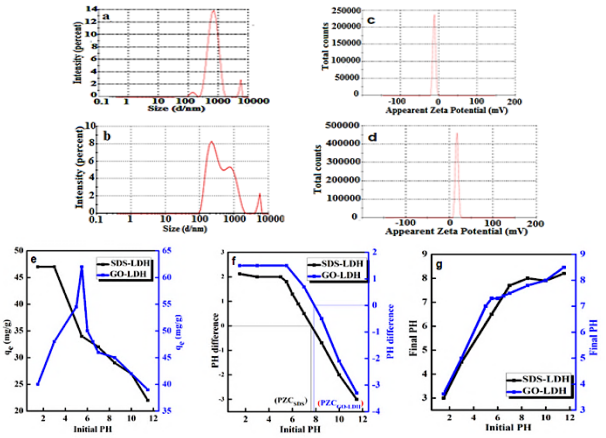

Fig. 6 - Zeta-sizer size distribution of a) SDS-LDH and b) GO-LDH, zeta-potential of c) SDS-LDH, d) GO-LDH, e) adsorption capacity vs pH of SDS-LDH (t=60 min, C_o= 40 ppm, dose= 85 mg, T= 20 ˚C) and GO-LDH (t= 10 min, C_o= 40, dose= 65 mg, at T=20˚C), f) pH difference vs initial pH and g) final pH vs initial pH for SDS-LDH and GO-LDH.

3.2. Adsorption, kinetics and isotherm studies

3.2.1. Contact time effect and adsorption kinetics

The adsorption capacity of CBB by the synthesized adsorbents varied as the adsorption time proceeded as displayed in Supp Fig. 3. The contact time effect of CBB adsorption was tested at 20˚C, 20 and 40 ppm initial concentration at pH= 7 and 5.5 for 65 mg dose of SDS-LDH and GO-LDH, respectively. The adsorption capacity was so steep to reach 46 and 53 mg/g for the first 10 min and 30 seconds then gradually slowed down to 51 and 62 mg/g till reaching equilibrium at 60 and 5 minutes for SDS-LDH and GO-LDH, respectively. The equilibrium state was due to the super saturation of the CBB on the adsorbents owing to the large interlayered distances of GO-LDH as well as its high surface area, which allowed the rapid diffusion of CBB molecules in a few minutes (Liang et al., 2015) as compared to SDS-LDH that relied on the solubility of CBB molecules with SDS alkyl chains "ad-solubilization process" (Munir et al., 2020), (Ramimoghadam, Hussein, & Taufiq-Yap, 2012). The mechanism of solid-phase adsorption was investigated via various kinetic models as: PFO (Benjelloun et al. (2021)), Bhattacharya and Venkobachar, Natarajan and Khalaf (Srihari & Das, 2008)], PSO, Avrami, Elovich Benjelloun et al. (2021), Ritchie (Bayramoğlu et al. (2006)), Fractional Power (Srihari & Das, 2008), Boyd ion exchange model, and intra-particle diffusion (Ni et al., 2007)], which were expressed by equations as explained in Supp Table 1.

Table 1 - Kinetic models for and experimental adsorption capacity of SDS-LDH and GO-LDH.

Model	Model Equations	Parameters	SDS-LDH	GO-LDH
PFO	$\ln(q_e-q_t) = \ln q_e - k_1 t$	$\mathbf{K_1}$ (min^{-1})	0.0342	0.5015
		$\boldsymbol{q_{e.cal}}$ (mg/g)	70.43	14.53
		$\mathbf{R^2}$	0.918	0.899
Bhattacharya and Venkobachar	$\ln(1-U(t)) = -K_b t$, $U(t)=\frac{C_o-C_t}{C_o-C_e}$	$\mathbf{K_b}$ (min^{-1})	0.03912	0.56777
		$\mathbf{R^2}$	0.9297	0.9367
Natarajan and Khalaf	$\mathrm{Ln}(\frac{C_o}{C_t}) = k_n t$	$\mathbf{K_n}$ (min^{-1})	0.0107	0.5386
		$\mathbf{R^2}$	0.992	0.9764
PSO	$\frac{t}{q_t} = \frac{1}{K_2 q_e^2} + \frac{t}{q_e}$, $h=k_2 qe^2$ (mg g^{-1} min^{-1})	$\mathbf{K_2}$ (g $mg^{-1}min^{-1}$)	0.0171	0.0768
		$\boldsymbol{q_{e.calc}}$(mg/g)	51.33	63.69
		$\mathbf{R^2}$	0.999	0.999
Avrami	$\ln(-\ln(1-q_t)) = \ln(k_{av}) + n_{av}\ln(t)$	$\mathbf{k_{av}}$ (min^{-1})	1.0825	2.0919
		$\mathbf{n_{av}}$	0.3052	0.3125
		$\mathbf{R^2}$	0.8234	0.7709
Elovich	$q_t = \frac{1}{\beta}\ln(\alpha\beta) - \frac{1}{\beta}\ln(t)$	$\boldsymbol{\beta}$ (mg/g)	0.366	0.256
		$\boldsymbol{\alpha}$ (mg/g min)	$1.163*10^{9}$	$1.308*10^{47}$
		$\mathbf{R^2}$	0.9203	0.8939
Ritchie	$\frac{1}{q_t} = \frac{1}{k_2 q_{eq} t} + \frac{1}{q_{eq}}$	$\mathbf{k_2}$ (g/mg.min)	1.055	23.21
		$\mathbf{q_{e\ cal}}$ (mg/g)	50.05	57.11
		$\mathbf{R^2}$	0.75597	0.76796
Fractional power	$\mathrm{Log}\ q_t = \log(a) + b\log(t)$	$\boldsymbol{\alpha}$	4.963	5.667
		$\boldsymbol{\beta}$	0.05657	0.06886
		$\mathbf{R^2}$	0.92808	0.90639
Boyd	$B_t = -0.4977 - \ln(1-\frac{q_t}{q_e})$	$\boldsymbol{\beta}$	0.039112	0.50159

	R^2	0.9298	0.8933
Experimental adsorption capacity	$q_{e\ exp}$	51	62

Table 1 showed that SDS-LDH obeyed Bhattacharya and Venkobachar with K_b (0.03912) min^{-1}, which well-matched with K_1 (0.0342) min^{-1} of PFO than GO-LDH with K_n (0.5386) min^{-1}, which obeyed Natarajan and Khalaf and agreed with K_1 (0.5015) min^{-1} of PFO. Furthermore, the adsorbate uptake by the adsorbent positively is correlated with β of fractional power for SDS-LDH (β=0.05657) and GO-LDH (β=0.06886) than that for Elovich. However, Avrami's and Ritchie's data revealed that the adsorption was instantaneous (n_{av}<1), obeying diffusive law and ion exchange, the observed low trend of R^2 for Avrami and Ritchie was not applicable for the adsorption system. PSO's kinetic model showed the best fit of all these models and suggested the physisorption nature. The adsorption mechanism was well-defined by Boyd's and the intra-particular diffusion model. Supp Table 1 displayed that Boyd's constant β= 0.039112 and 0.50159 with R^2 = 0.9298 and 0.8933 for SDS-LDH and GO-LDH, respectively, didn't pass the origin. Therefore, not only the film extra-particular diffusion but also intra-particle diffusion was the predominant and the later was the most effective (inner transport > outer transport). The mechanism was demonstrated according to the intra-particle diffusion model that depicted the presence of three linear regions as shown in Supp Fig. 3 (Rashed et al., 2022), (Ni et al., 2007). The first region described the film diffusion, demonstrating the dye diffused from the solution to the external surface of either SDS-LDH or GO-LDH with an increased diffusion constant 14.577 and 74.9647 $mg/g.min^{-1}$ for SDS-LDH and GO-LDH, respectively, along with zero boundary layer thickness for the both adsorbents, as presented in Supp Table 2. The second region described the intra-particle diffusion, referring to dye molecules diffusion via the layers of SDS-LDH and GO-LDH with diffusion constant of 1.22 and 6.275 $mg/g.min^{-1}$, respectively and then reduced to zero due to the saturation of dye molecules in the third region via intra-particle diffusion, as shown in Supp Table 2. In the second and third region of CBB adsorption, the boundary layer thickness increased till reaching equilibrium of SDS-LDH (41.418 and 51 mg/g) and GO-LDH (47.347 and 62 mg/g), respectively, Supp. Table 2.

Table 2 - Intra-particle diffusion of SDS-LDH and GO-LDH.

Intra-particle diffusion of SDS-LDH		$q_t = k_i t^{1/2} + C$	
	K_{IP} (mg/g min^{-1})	**C (mg/g)**	**R^2**
Region 1	**14.577**	**0**	**-**
Region 2	**1.22**	**41.418**	**0.99177**
Region 3	**0**	**51**	**-**
Intra-particle diffusion of GO-LDH		$q_t = k_i t^{1/2} + C$	
Region 1	**74.9647**	**0**	**-**
Region 2	**6.275**	**47.347**	**0.9876**
Region 3	**0**	**62**	**-**

Furthermore, as the boundary layer thickness increased, intra-particle diffusion was not the only rate-determining step (Rashed et al., 2022) as illustrated in Supp Fig. 3

3.2.2. Initial dye concentration effect and equilibrium data

The increase in adsorption capacity curve with increasing initial concentrations of CBB (20-100 and 40-200 mg/L) for SDS-LDH (26-57 mg/g) and GO-LDH (60-263 mg/g), respectively was displayed in Fig. 10a. The adsorption capacity of GO-LDH was vastly larger than that of SDS-LDH as the higher mass driving force of high concentration was directed towards the available high interlayered distance, allowing super CBB adsorption and intercalation (Munir et al., 2020). Demonstratively, SDS-LDH lacked GO-LDH properties, so the hydrophobic interaction with CBB was not effective as the ion-exchange of GO-LDH with CBB. The isothermal behaviour associated with solid-liquid adsorption dynamics was investigated through a comprehensive suite of isotherm models. These encompassed the classical Langmuir and Freundlich models, along with the Harkins-Jura Benjelloun et al. (2021), Jovanovi (Ayawei et al., 2017), Sips, Flory-Huggins, Brunauer-Emmett-Teller, Dubinin-Radushkevich (D-R), and Redlich-Peterson isotherms Benjelloun et al. (2021). An intricate analysis and discussion pertaining to the underlying adsorption mechanisms, as well as the affinity characterizations of the adsorbents, have been delineated in the supplementary information section. The adsorption isotherms plots were displayed in Fig. 8(b-k) and their equilibrium data, based on R^2, and adsorption parameters were recorded and calculated in Supp Table 3. According to R^2, the adsorption system lied between the homogenous monolayered and heterogenous multilayered adsorption with arrangement order Langmuir>Redlich-Peterson>Sips>Freundlich>Florry-Huggins>Harkins-Jura>Dubinin-Radushkevich>Bruaner-emmet teller>Jovanovic and Harkins-Jura>Redlich-Peterson>Jovanovic>Freundlich>Langmuir>Bruaner-emmetteller>Florry-Huggins>Sips>Dubinin Radushkevich for SDS-LDH and GO-LDH, respectively. SDS-LDH was observed to perfectly fit Langmuir isotherm with maximum adsorption capacity of (q_m =60 mg/g) of homogenously monolayered coverage with the prove of Redlich-Peterson of (β= 0.7435 Lmg^{-1}) close to unity more than that of GO-LDH (q_m=333.33 mg/g,

β=0.59201 Lmg^{-1}). The Langmuir isotherm is eloquently characterized by the dimensionless separation factor, (R_L), as illustrated in Fig. 8c. R_L values of the initial concentration of CBB of SDS-LDH (0.2016 - 0.0481 mg/L) and GO-LDH (0.0646 - 0.0269 mg/L) lied between 0 and 1, referring to strong adsorption due to the low R_L values (Ai, et al 2011). Moreover, the sips isotherm possessed q_{max} = 64.505 mg/g with Freundlich adsorption intensity 1/n= 0.255 mg/L. The positive Flory-Huggins k_d indicated that the system was spontaneous and feasible. The harkins-jura, Dubinin Radushkevich, Bruaner-emmet-teller, and javonovic isotherms didn't take part in the SDS-LDH adsorption system, based on small R^2. On the other hand, GO-LDH was found to perfectly fit the Harkins-Jura isotherm (A= 17336, B= 1.692), with Redlich Peterson of β of GO-LDH (0.59201 Lmg^{-1}), which is decreased due to the high initial concentration of CBB dye obeying Jovanovic isotherm of q_{max}= 111.084 mg/g, exhibiting mechanical interaction between the adsorbent and the adsorbate, and Freundlich isotherm of adsorption intensity (1/n) of 0.4076 mg/L. The Bruaner-emmet-teller, flory huggins, sips, and D-R weren't involved in the adsorption system of GO-LDH, based on small R^2. Hence, it was obvious that SDS-LDH preferred the monolayered adsorption (homogenous nature), while, GO-LDH favored the multilayered adsorption (heterogeneity nature), as discussed in the schematic diagram Fig. 8.

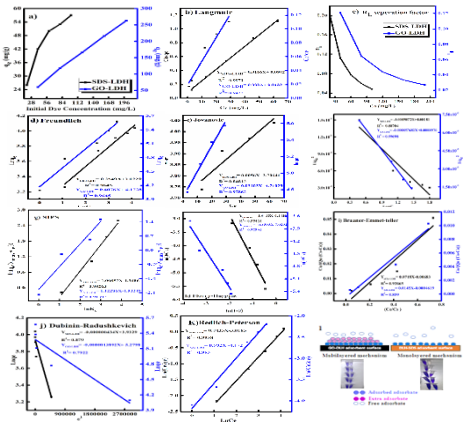

Fig. 7 - a) Effect of initial concentration of SDS-LDH (PH= 7, t=60 min, dose= 65 mg, T=20 °C) and GO-LDH (PH= 5.5, t= 5 min, dose= 65 mg, T= 20 °C), Adsorption isotherms of b) Langmuir, c) R_L separation factor, d) Freundlich, e) Harkins-Jura, f) Jovanovic, g) SIPS, h) Florry-Huggins, i) Bruaner-Emmet-teller, j) Dubinin-Radushkevich, k) Redlich-Peterson and l) schematic diagram of multi- and monolayered adsorption mechanism

Table 3. Adsorption isotherms calculations of CBB molecules onto SDS-LDH and GO-LDH

Isotherms	Equations	parameters	SDS-LDH	GO-LDH
Langmuir	$\frac{C_e}{q_e} = \frac{1}{q_m K_L} + \frac{C_e}{q_m}$, $R_L = \frac{1}{1+k_l C_o}$	q_m (mg/g)	60	333.33
		K_L (mg/L)	0.198	0.1814
		R^2	0.9971	0.942
Freundlich	Ln q_e= Ln K_f + $\frac{1}{n}$ Ln C_e	K_F (mg/g) (mg/L)$^{1/n}$	20.677	64.91
		1/n (mg/L)	0.255	0.4076
		n (L/mg)	3.92	2.4535
		R^2	0.9645	0.9645
Harkins-Jura	$\frac{1}{q_e^2} = \frac{B}{A} - \frac{1}{A}\log Ce$	A	1102	17336
		B	1.995	1.692
		R^2	0.88704	0.99698
Jovanovic	ln q_e = ln q_{max} - k_j C_e	q_{max} (mg/g)	40.707	111.084
		k_j (Lg^{-1})	0.0056	0.031
		R^2	0.84812	0.97862
Sips	$\ln(\frac{q_e}{q_{max}-q_e}) = \frac{1}{n}\ln C_e + \ln k_s$	n	0.992	0.891
		k_s (Lg^{-1})	0.254	0.145
		q_{max} (mg/g)	64.505 0.9826	304.41
		R^2		0.91397
Florry-Huggins	ln $\frac{\theta}{C_e}$ = ln (K_{FH}) + α_{FH} ln(1-θ)	α_{FH}	-1.64148	-0.85935
		K_{FH} (mg/g)	$2.153*10^{-3}$	$8.937*10^{-4}$
		R^2	0.95426	0.92961
Bruaner-Emmet-teller	$\frac{C_e}{Q_e(C_s - C_e)} = \frac{1}{Q_s C_{BET}} + \frac{(C_{BET}-1)(\frac{C_e}{C_s})}{Q_s C_{BET}}$	Q_s (mg/g)	21.901	336.958
		C_{BET} (L/mg)	-0.0556	0.107
		R^2	0.859	0.93665
Dubinin-Radushkevich	ln q_e= ln q_m - βε^2 , ε= RT ln (1+$\frac{1}{C_e}$),	β ($mol^2 kJ^{-2}$)	$4.34*10^{-7}$	$1.389*10^{-6}$
		q_m (mg/g)	51.053	196.33

	$E=(\frac{1}{2\beta})^{\frac{-1}{2}}$	E (kJ mol^{-1})	2.946*10^{-3}	9.317*10^{-4}
		R^2	0.88	0.7922
Redlich - Peterson	$ln\frac{C_e}{q_e} = \beta \ln C_e - lnA$	β (Lmg^{-1})	0.7435	0.59201
		A (Lg^{-1})	0.0489	0.0154
		R^2	0.9958	0.983

3.2.3. Adsorbent dose effect

The adsorption capacity was investigated by varying the adsorbent dose as shown in Fig. 9. The adsorption capacities of SDS-LDH (53-26 mg/g) and GO-LDH (2646 -73 mg/g) curves were observed to decrease as the adsorbent dose of SDS-LDH (25-105 mg) and GO-LDH (2.5-105 mg) increased. It was found that increasing the dose of either SDS-LDH or GO-LDH adsorbents led to their aggregation, causing the surface area degradation and resulting in low adsorption capacity. However, as the dose of SDS-LDH or GO-LDH decreased, the phases of the adsorbents were easily dispersed, allowing an ease CBB adsorption **(Rashed et al., 2022)**. Illustratively, 5 mg of GO-LDH resulted in an adsorption capacity of 1443 mg/g, which was consistent with results obtained by TMGO (7 mg) for the removal of CBB dye [3].

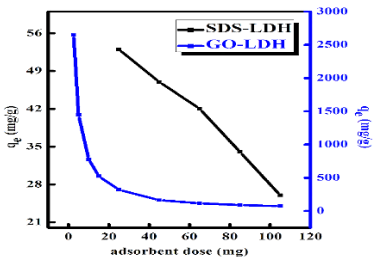

Fig. 8 - Effect of adsorbent dose: SDS-LDH (PH= 7, t=60 min, C_o = 40 ppm, T= 20 ˚C) and GO-LDH (PH= 5.5, t=5 min, C_o = 80 ppm, T= 20 ˚C).

3.2.4. Sodium Chloride effect

In the realm of adsorption dynamics, ionic potency is a critical factor that can exhibit an ascending, descending, or steady trend. Evidently, as delineated in Fig. 10, the escalation in sodium chloride concentrations (from 20 to 100 mg) exhibited no discernible alteration in the adsorptive capabilities of SDS-LDH, which steadfastly stood at 41 mg/g. However, a palpable decline in the GO-LDH adsorptive prowess was observed, plummeting from 1240 mg/g to a diminished 870 mg/g. This decrement can be attributed to the repulsive interplay between the negative valences of chloride ions and those of CBB anions, which inevitably curtailed the adsorptive competence of GO-LDH. Contrarily, such electrostatic repulsions bore no influence on the hydrophobic exchanges characterizing the SDS-LDH and CBB liaison (Rashed et al., 2022), (Danaei et al., 2018), (Simonin, 2016)].

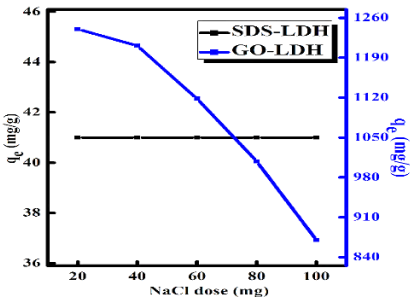

Fig. 9 - NaCl dose effect for SDS-LDH (PH=3, t=60 min, C_o =40 ppm, dose=85 mg, T=20˚C) and GO-LDH (PH=5.5, t=5 min, C_o =80 ppm, dose=5 mg, T=20 ˚C).

3.2.5. Temperature effect and thermodynamic studies

The temperature parameter effect on adsorption capacity was displayed in Fig. 11a. As the temperature increased (20°C–80°C), the adsorption capacity reduced for SDS-LDH (47–24 mg/g) and for GO-LDH (1443–1168 mg/g). This may be due to the weakened attractive forces between CBB and SDS-LDH/GO-LDH, allowing the escape of CBB molecules from the solid phase to the liquid phase, thus the adsorption process could be physical adsorption (Abbas et al., 2016). The temperature effect on CBB adsorption by SDS-LDH or GO-LDH was thermodynamically explained to determine the standard enthalpy (ΔH°), standard entropy (ΔS°), and standard free Gibb's energy (ΔG°), using Vant's Hoff equation (Rashed et al., 2022) as displayed in Fig. 11b and Table 4. The entropy was found to possess negative values (Table 4), indicating that the randomness decreased and CBB molecule adsorption on SDS-LDH or GO-LDH was restricted. In addition, negative enthalpy values referred to exothermic adsorption process. Besides, the increase in negativity of Gibb's

free energy was corresponding to CBB spontaneous adsorption by either SDS-LDH or GO-LDH (Ibrahim et al., 2019), (Sen et al., 2012)].

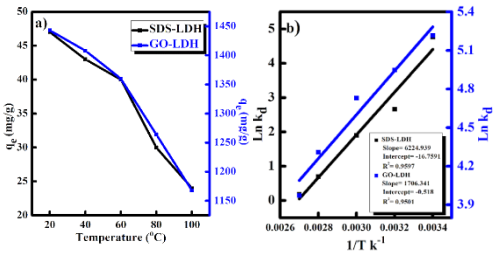

Fig. 10 - a) Effect of temperature on SDS-LDH (PH=3, t=60 min, C_o =40 ppm, dose=85 mg) and GO-LDH (PH 5.5, t= 5 min, C_o =80 ppm, dose=5 mg) and b) van't hoff plot image.

Table 4. Thermodynamic values for CBB (G-250) dye adsorption onto SDS-LDH and GO-LDH

TEMPERATURE (K)	ENTROPY (J/MOL.K^{-1})	ENTHALPY (KJ/MOL)	FREE GIBBS ENERGY (KJ/MOL)	K_D
	SDS-LDH			
298	-139.3	-51.75	-10.92889	88.8
313	-139.3	-51.75	-5.9456969	22.84
328	-139.3	-51.75	-5.35548	6.92
343	-139.3	-51.75	-2.568773	2.4
358	-139.3	-51.75	0.218	0.932
GO-LDH				
298	-4.306	-14.19	-12.9248	201.49
313	-4.306	-14.19	-12.83867	138.88
328	-4.306	-14.19	-12.75255	100.1
343	-4.306	-14.19	-12.66642	74.88
358	-4.306	-14.19	-12.5803	57.78

3.3. Recycling and regeneration studies

LDHs are very important economically in water treatment studies because they can be reused after dye adsorption. Fig. 12a showed the reusability of SDS-LDH and GO-LDH after CBB dye adsorption using the "memory effect" (Starukh et al., 2016), (Starukh & Levytska, 2019),(Mishra, et al., 2018). CBB/SDS-LDH and CBB/GO-LDH were calcined by combustion at 350 ºC for 1 hour to remove the adsorbed CBB dye, resulting in calcined double layered hydroxides (C-LDH) and calcined reduced graphene oxide double layered hydroxides (C-RGO-LDH), respectively. The adsorption capacity of C-LDH (47-8 mg/g) and C-RGO-LDH (1443-1320 mg/g) decreased after 5 cycles. Ulibarri et al reported that the reduction in adsorption capacity by C-LDH was due to the elimination of SDS and poor crystallinity caused by calcination, resulting in decreasing dispersion and surface area (Ni et al., 2007). On the contrary, the calcination process had no effect on the properties of C-RGO-LDH that affected the C-LDH. Besides, the high adsorption recycling confirmed that the GO-LDH surface was heterogeneous, obeying the multilayered mechanism and well matched the Harkins-Jura isotherm. The schematic diagrams of Fig. 12b explained the mechanism of regeneration process via memory effect of the tested adsorbents.

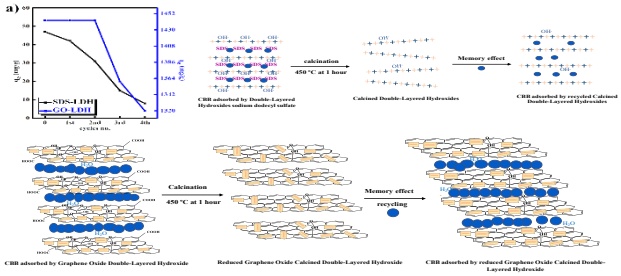

Fig. 11 - a) Cycles numbers of regenerated CBB dye adsorption by SDS-LDH (PH= 3, t= 60 min, C_o= 40 ppm dose= 65 mg, T= 20˚C) and GO-LDH (PH= 5.5, t= 5 min, C_o= 80 ppm, dose=5 mg, T= 20˚C) and Schematic diagrams of memory effect of b) SDS-LDH and c) GO-LDH.

4. Conclusion

In this context the synthesis of SDS-LDH and GO-LDH via the reconstruction method and the sonochemical method, respectively, for the elimination of CBB organic dye pollutants from an aqueous solution was studied. The morphology of SDS-LDH and GO-LDH were shown to be lamellar structured with a specific average surface area of $35.5*10^6$ nm^2/g and $47*10^6$ nm^2/g, as well as polydispersity index of 0.34 and 0.406, and an interlamellar distance of 8.8 Å and 11.043 Å, respectively, proving the high element purity of Zn, Al, C, O, and Na. CBB adsorption mechanisms of SDS-LDH and GO-LDH were via hydrophobic interaction and ion-exchange, respectively, inducing better thermal stability of CBB by GO-LDH than SDS-LDH with weight loss of 0.269 mg and 0.699 mg, respectively. Accordingly, at room temperature, the q_e of GO-LDH (1443 mg/g) at (pH = 5.5, t= 5 mins, C_o= 80 ppm, dose = 5 mg) was higher than that of SDS-LDH (62 mg/g) at (pH = 3, t= 60 mins, C_o= 40 ppm, dose = 85 mg), following the PSO kinetic model with initial velocity 45.167 mg g^{-1} min^{-1} and 311.526 mg g^{-1} min^{-1} for SDS-LDH and GO-LDH, respectively and controlled by the film and intra-particle diffusion mechanism. Additionally, SDS-LDH and GO-LDH follow the monolayered mechanism of the Langmuir isotherm and the multilayered mechanism of the Harkins-Jura isotherm, respectively. The CBB adsorption process was restricted (-ΔS°), exothermic (-ΔH°), spontaneous (-ΔG°), and physical. Using the memory effect of the adsorbents, C-LDH and RGO-C-LDH were recycled, showing that RGO-C-LDH (1443-1320 mg/g) was more efficient than that of C-LDH (47-8 mg/g) after five runs. These results show that GO-LDH was sustainable adsorbent because of its nearly zero-cost production in the wastewater industry.

Acknowledgements

The authors would like to acknowledge Faculty of Science, Alexandria University for their support to make this research possible.

Conflict of Interest

The authors declare no conflict of interest.

References:

Abbas, M., Cherfi, A., Kaddour, S., & Aksil, T. (2016). Adsorption in simple batch experiments of Coomassie blue G-250 by apricot stone activated carbon—Kinetics and isotherms modelling. *Desalination and Water Treatment, 57*, 15037–15048. https://doi.org/10.1080/19443994.2015.1067871

Abd-Elhamid, A. I., Eltaweil, A. S., Elgarahy, A. M., & El-Subruiti, G. M. (2019). Decontamination of organic pollutants from aqueous media using cotton fiber–graphene oxide composite, utilizing batch and filter adsorption techniques: A comparative study. *RSC Advances, 9*, 5770–5785. https://doi.org/10.1039/C8RA10449B

Abdel-Ghani, N. T., Hefny, M., El-Chaghaby, G. A., & El-Gendy, N. S. (2017). Adsorption of Coomassie brilliant blue R-250 dye onto novel activated carbon prepared from *Nigella sativa* L. waste: Equilibrium, kinetics and thermodynamics. *Journal of the Chilean Chemical Society, 62*, 3505–3511. https://doi.org/10.4067/S0717-97072017000200016

Abu-Nada, A., Abdala, A., & McKay, G. (2021). Removal of phenols and dyes from aqueous solutions using graphene and graphene composite adsorption: A review. *Journal of Environmental Chemical Engineering, 9*, 105858. https://doi.org/10.1016/j.jece.2021.105858

Abzalov, M. (2008). Quality control of assay data: a review of procedures for measuring and monitoring precision and accuracy. Exploration and Mining Geology, 17(3-4), 131-144. https://doi.org/10.2113/gsemg.17.3-4.131

Ai, L., Zhang, C., & Meng, L. (2011). Adsorption of methyl orange from aqueous solution on hydrothermal synthesized Mg–Al layered double hydroxide. *Journal of Chemical & Engineering Data, 56*, 4217–4225. https://doi.org/10.1021/je200743u

Ata, S., Ahmed, A., & Shah, S. S. (2012). Equilibrium, thermodynamics, and kinetic sorption studies for the removal of Coomassie Brilliant Blue on wheat bran as a low-cost adsorbent. *Journal of Analytical Methods in Chemistry, 2012*, 405980. https://doi.org/10.1155/2012/405980

Ayawei, N., Ebelegi, A. N., & Wankasi, D. (2017). Modelling and interpretation of adsorption isotherms. *Journal of Chemistry, 2017*, 1–11. https://doi.org/10.1155/2017/3039817

Bayramoğlu, G., Çelik, G., & Arica, M. Y. (2006). Biosorption of Reactive Blue 4 dye by native and treated fungus *Phanerochaete chrysosporium*: Batch and continuous flow system studies. *Journal of Hazardous Materials, 137*, 1689–1697. https://doi.org/10.1016/j.jhazmat.2006.05.005

Benjelloun, M., Miyah, Y., Lairini, S., & Bouch, J. (2021). Recent advances in adsorption kinetic models: Their application to dye types. *Arabian Journal of Chemistry, 14*, 103031. https://doi.org/10.1016/j.arabjc.2021.103031

Bhavyasree, P. G., & Xavier, T. S. (2021). Adsorption studies of methylene blue, Coomassie brilliant blue, and Congo red dyes onto CuO/C nanocomposites synthesized via *Vitex negundo* Linn leaf extract. *Current Research in Green and Sustainable Chemistry, 4*, 100161. https://doi.org/10.1016/j.crgsc.2021.100161

Bu, J., Yuan, L., Zhang, N., Meng, Y., & Peng, X. (2021). Novel adsorbent of N-phenylthiourea-functionalized graphene oxide and its removal of methyl orange in aqueous solutions. *Journal of Chemical & Engineering Data, 66*, 199–209. https://doi.org/10.1021/acs.jced.0c00527

Danaei, M., Dehghankhold, M., Ataei, S., Hasanzadeh Davarani, F., Javanmard, R., Dokhani, A., Khorasani, S., & Mozafari, M. R. (2018). Impact of particle size and polydispersity index on the clinical applications of lipidic nanocarrier systems. *Pharmaceutics, 10*, 57. https://doi.org/10.3390/pharmaceutics10020057

Daud, M., Nafees, M., & Ali, A. (2019). A review on the recent advances, challenges and future aspect of layered double hydroxides (LDH)-containing hybrids as promising adsorbents for dyes removal. *Journal of Molecular Liquids, 288*, 110989. https://doi.org/10.1016/j.molliq.2019.110989

Dhananasekaran, S., Palanivel, R., & Pappu, S. (2016). Adsorption of methylene blue, bromophenol blue, and Coomassie brilliant blue by α-chitin nanoparticles. *Journal of Advanced Research, 7*, 113–124. https://doi.org/10.1016/j.jare.2015.03.003

Elmoubarki, R., Elhalil, A., Farnane, M., Mahjoubi, F. Z., & Barka, N. (2021). Ni-Fe-SDS and Ni-Fe-SO_4 layered double hydroxides: Preparation, characterization and application in dyes removal. *Materials Today: Proceedings, 37*, 3871–3875. https://doi.org/10.1016/j.matpr.2020.08.460

Gohr, M. S., Ibrahim, M., & Abdelwahab, M. A. (2022). Adsorption of cationic dyes onto chemically modified activated carbon: Kinetics and thermodynamic study. *Journal of Molecular Liquids, 346*, 118227. https://doi.org/10.1016/j.molliq.2021.118227

Gohr, M. S., Ibrahim, M., & Abdelwahab, M. A. (2019). Facile hydrothermal synthesis of Sm and Eu doped TiO_2/graphene oxide nanocomposites for photocatalytic applications. *Egyptian Journal of Chemistry*. https://doi.org/10.21608/ejchem.2019.15112.1914

Gupta, N. K., Rajoriya, S., Vijay, Y. K., & Sahu, K. K. (2023). Zinc–aluminum layered double hydroxide and double oxide for room-temperature oxidation of sulfur dioxide gas. *Chemosphere, 338*, 139503. https://doi.org/10.1016/j.chemosphere.2023.139503

Ibrahim, H. K., Ali, S. A., & Rahiem, S. S. A. (2019). Decolorization of Coomassie brilliant blue G-250 dye using snail shell powder by action of adsorption processes. *Research Journal of Pharmacy and Technology, 12*, 4921. https://doi.org/10.5958/0974-360X.2019.00853.9

Jawad, S. F., Rahim, A. F. A., Abdulmohsin, A. A., & Zaini, M. A. A. (2021). Dye removal from textile wastewater using solar-powered electrocoagulation reactor. *IOP Conference Series: Materials Science and Engineering, 1058*, 012016. https://doi.org/10.1088/1757-899X/1058/1/012016

Kadeche, A., Berred jem, A., & Sahraoui, S. (2020). Preparation, characterization and application of Fe-pillared bentonite to the removal of Coomassie blue dye from aqueous solutions. *Research on Chemical Intermediates, 46*, 4985–5008. https://doi.org/10.1007/s11164-020-04236-2

Kong, Y., Wang, X., Zhao, Y., Liu, H., & Zhou, M. (2018). Sodium dodecylsulfate-layered double hydroxide and its use in the adsorption of 17β-estradiol in wastewater. *RSC Advances, 8*, 31440–31454. https://doi.org/10.1039/C8RA05726E

Liang, A., Luo, X., Wen, G., & Jiang, Z. (2015). SERS quantitative analysis of trace HSA with a Coomassie brilliant blue G-250 molecular probe in nanogold sol substrate. *RSC Advances, 5*, 5711–5715. https://doi.org/10.1039/C4RA11778F

Lin, Y., Fang, Q., & Chen, B. (2014). Perchlorate uptake and molecular mechanisms by magnesium/aluminum carbonate layered double hydroxides and the calcined layered double hydroxides. *Chemical Engineering Journal, 237*, 38–46. https://doi.org/10.1016/j.cej.2013.10.004

Liu, Y., Li, X., Zhang, B., Wang, J., & Yang, J. (2015). Degradation of the common aqueous antibiotic tetracycline using a carbon nanotube electrochemical filter. *Environmental Science & Technology, 49*, 7974–7980. https://doi.org/10.1021/acs.est.5b00870

Lü, X., Zhang, Y., Liu, Y., Zhu, Y., & Wang, Y. (2007). Application of a modified Coomassie brilliant blue protein assay in the study of protein adsorption on carbon thin films. *Surface and Coatings Technology, 201*, 6843–6846. https://doi.org/10.1016/j.surfcoat.2006.09.019

Mahjoubi, F. Z., Elmoubarki, R., Farnane, M., & Barka, N. (2019). Characteristics and mechanisms of methyl orange sorption onto Zn/Al layered double hydroxide intercalated by dodecyl sulfate anion. *Scientific African, 6*, e00216. https://doi.org/10.1016/j.sciaf.2019.e00216

Mishra, G., Dash, B., & Pandey, S. (2018). Layered double hydroxides: A brief review from fundamentals to application as evolving biomaterials. *Applied Clay Science, 153*, 172–186. https://doi.org/10.1016/j.clay.2017.12.021

Munir, M., Shakoor, M. B., Anwar, M. M., Ali, U., & Saeed, M. (2020). Effective adsorptive removal of methylene blue from water by didodecyldimethylammonium bromide-modified brown clay. *ACS Omega, 5*, 16711–16721. https://doi.org/10.1021/acsomega.0c01613

Ni, Z.-M., Xia, S.-J., Wang, L.-G., Xing, F.-F., & Pan, G.-X. (2007). Treatment of methyl orange by calcined layered double hydroxides in aqueous solution: Adsorption property and kinetic studies. *Journal of Colloid and Interface Science, 316*, 284–291. https://doi.org/10.1016/j.jcis.2007.07.045

Ramimoghadam, D., Hussein, M. Z., & Taufiq-Yap, Y. H. (2012). The effect of sodium dodecyl sulfate (SDS) and cetyltrimethylammonium bromide (CTAB) on the properties of ZnO synthesized by hydrothermal method. *International Journal of Molecular Sciences, 13*, 13275–13293. https://doi.org/10.3390/ijms131013275

Rashed, S. H., El-Sayed, M. A., Abdel-Halim, E. S., & El-Naggar, M. E. (2022). Preparation and characterization of layered-double hydroxides decorated on graphene oxide for dye removal from aqueous solution. *Journal of Materials Research and Technology, 17*, 2782–2795. https://doi.org/10.1016/j.jmrt.2022.02.040

Rauf, M. A., Bukallah, S. B., Hamour, F. A., & Nasir, A. S. (2008). Adsorption of dyes from aqueous solutions onto sand and their kinetic behavior. *Chemical Engineering Journal, 137*, 238–243. https://doi.org/10.1016/j.cej.2007.04.025

Rayaroth, M. P., Aravind, U. K., Aravindakumar, C. T., & Pandey, A. (2015). Sonochemical degradation of Coomassie Brilliant Blue: Effect of frequency, power density, pH and various additives. *Chemosphere, 119*, 848–855. https://doi.org/10.1016/j.chemosphere.2014.08.037

Sabeela, N. I., Joseph, J., & Anas, A. (2019). Reactive mesoporous pH-sensitive amino-functionalized silica nanoparticles for efficient removal of Coomassie Blue dye. *Nanomaterials, 9*, 1721. https://doi.org/10.3390/nano9121721

Sen, T. K., Thi, M. T., Afroze, S., Phan, C., & Ang, M. (2012). Removal of anionic surfactant sodium dodecyl sulphate from aqueous solution by adsorption onto pine cone biomass of *Pinus radiata*: Equilibrium, thermodynamic, kinetics, mechanism and process design. *Desalination and Water Treatment, 45*, 263–275. https://doi.org/10.1080/19443994.2012.691699

Sharif, S. N. M., Hussein, M. Z., Zainal, Z., Taufiq-Yap, Y. H., & Al Ali, S. H. (2020). Controlled release formulation of zinc hydroxide nitrate intercalated with sodium dodecylsulphate and bispyribac anions: A novel herbicide nanocomposite for paddy cultivation. *Arabian Journal of Chemistry, 13*, 4513–4527. https://doi.org/10.1016/j.arabjc.2019.09.006

Sharma, G., Naushad, M., Pathania, D., & Kumar, A. (2017). Efficient removal of Coomassie brilliant blue R-250 dye using starch/poly(alginic acid-cl-acrylamide) nanohydrogel. *Process Safety and Environmental Protection, 109*, 301–310. https://doi.org/10.1016/j.psep.2017.04.011

Simonin, J.-P. (2016). On the comparison of pseudo-first order and pseudo-second order rate laws in the modeling of adsorption kinetics. *Chemical Engineering Journal, 300*, 254–263. https://doi.org/10.1016/j.cej.2016.04.079

Srihari, V., & Das, A. (2008). The kinetic and thermodynamic studies of phenol-sorption onto three agro-based carbons. *Desalination, 225*, 220–234. https://doi.org/10.1016/j.desal.2007.07.008

Starukh, G., Rozovik, O., & Oranska, O. (2016). Organo/Zn-Al LDH nanocomposites for cationic dye removal from aqueous media. *Nanoscale Research Letters, 11*, 228. https://doi.org/10.1186/s11671-016-1402-0

Starukh, H., & Levytska, S. (2019). The simultaneous anionic and cationic dyes removal with Zn-Al layered double hydroxides. *Applied Clay Science, 180*, 105183. https://doi.org/10.1016/j.clay.2019.105183

Stodden, V., McNutt, M., Bailey, D. H., Deelman, E., Gil, Y., Hanson, B., ... & Taufer, M. (2016). Enhancing reproducibility for computational methods. Science, 354(6317), 1240-1241.

Sujitha, R., & Ravindhranath, K. (2016). Removal of Coomassie brilliant blue dye from waste waters using active carbon derived from barks of *Ficus racemosa* plant. *Der Pharmacia Lettre, 8*, 72–83.

Tabana, L., Booysens, D.-R., & Tichapondwa, S. (2023). Photocatalytic degradation of efavirenz and nevirapine using visible light-activated Ag–AgBr–LDH nanocomposite catalyst. *Journal of Photochemistry and Photobiology A: Chemistry, 444*, 114997. https://doi.org/10.1016/j.jphotochem.2023.114997

Tang, Y., Li, Z., Wang, X., Zhou, Y., Liu, J., & Wang, Y. (2023). Facile synthesis of magnetic ZnAl layered double hydroxides and efficient adsorption of malachite green and Congo red. *Separation and Purification Technology, 322*, 124305. https://doi.org/10.1016/j.seppur.2023.124305

Tian, X., Liu, C., Chen, L., Zhang, M., & Liu, Z. (2023). Preparation of paramagnetic ferroferric oxide-calcined layered double hydroxide core–shell adsorbent for selective removal of anionic pollutants. *Journal of Colloid and Interface Science, 645*, 319–328. https://doi.org/10.1016/j.jcis.2023.04.151

Yilmaz, M. S. (2022). Graphene oxide/hollow mesoporous silica composite for selective adsorption of methylene blue. *Microporous and Mesoporous Materials, 330*, 111570. https://doi.org/10.1016/j.micromeso.2021.111570

Zaghouane-Boudiaf, H., Boutahala, M., & Arab, L. (2012). Removal of methyl orange from aqueous solution by uncalcined and calcined MgNiAl layered double hydroxides (LDHs). *Chemical Engineering Journal, 187*, 142–149. https://doi.org/10.1016/j.cej.2012.01.112

Zhang, M., Yang, D., Wang, C., Liu, Z., & Xu, H. (2019). Nickel–iron layered double hydroxides and reduced graphene oxide composite with robust lithium ion adsorption ability for high-capacity energy storage systems. *Electrochimica Acta, 296*, 190–197. https://doi.org/10.1016/j.electacta.2018.11.058

Zhao, B., Liu, Y., Wang, C., Zhang, X., Zhang, J., & Zhu, M. (2023). Laminated MXene foam/cellulose@LDH composite membrane with efficient EMI shielding property for asymmetric personal thermal management. *ACS Applied Materials & Interfaces, 15*, 8751–8760. https://doi.org/10.1021/acsami.2c21694